

## REPORT DOCUMENTATION PAGE

AFRL-SR-AR-TR-02-

0241

Public reporting burden for this collection of information is estimated to average 1 hour per response, including gathering and maintaining the data needed, and completing and reviewing the collection of information. Send collection of information, including suggestions for reducing this burden, to Washington Headquarters Services, Directorate for Information Operations and Reports, 1215 Jefferson Davis Highway, Suite 1204, Arlington, VA 22202-4302, and to the Office of Management and Budget, Paperwork Project, Washington, DC 20503.

1. AGENCY USE ONLY (Leave blank)	2. REPORT DATE 24 JUN 2002	3. REPORT TYPE AND DATES COVERED FINAL (01 DEC 99 TO 31 AUG 01)	
4. TITLE AND SUBTITLE CONTROLLED EXPERIMENTS ON INSTABILITIES AND TRANSITION TO TURBULENCE ON ELLIPTIC CONES AT HYPERSONIC MACH NUMBERS		5. FUNDING NUMBERS F49620-00-1-0074	
6. AUTHOR(S) PROFESSOR THOMAS C. COOKE			
7. PERFORMING ORGANIZATION NAME(S) AND ADDRESS(ES) UNIVERSITY OF NOTRE DAME AEROSPACE AND MECHANICAL ENGINEERING DEPARTMENT NOTRE DAME, IN 46556		8. PERFORMING ORGANIZATION REPORT NUMBER	
9. SPONSORING/MONITORING AGENCY NAME(S) AND ADDRESS(ES) AIR FORCE OFFICE OF SCIENTIFIC RESEARCH 801 N. RANDOLPH STREET ARLINGTON, VA 22203		10. SPONSORING/MONITORING AGENCY REPORT NUMBER	
11. SUPPLEMENTARY NOTES			
12a. DISTRIBUTION AVAILABILITY STATEMENT  Approved for public release; distribution unlimited.			
13. ABSTRACT (Maximum 200 words) This work involved the study of instabilities and transition to turbulence in boundary layers on cones at different angles of attacks at high supersonic and hypersonic Mach numbers. It utilized facilities at NASA Langley Research Center, which makes use of "quiet" design nozzles to minimize the level of acoustic disturbances. The experiments involved two models. The first was a 7 half-angle circular cross-section cone designed by Cavalier [1]. It was used in experiments at zero angle of attack [2,3], where the principle instability is pairs of traveling oblique wave pairs; and at angles of attack where the principle instability is cross-flow modes. The circular cone at an angle of attack has a 3-D boundary layer, which is similar to that on elliptic cone, which was the second model built. This consisted of a 10 half-angle cone with a 4:1 elliptic cross-section. The elliptic cone was designed to operate in a new Mach 8 tunnel at NASA Langley. It mounts on a sting, which placed it inside the worst-case estimate on the location of the nozzle quiet zone. The model is annealed and hardened to withstand the 900 F free-stream temperature, and maintain a polished finish. A 3-D traversing mechanism capable of following the tapered elliptic surface, and operating at high temperatures in the hypersonic flow was also designed [4]. Unfortunately, the elliptic cone was never used because of technical problems with the Mach 8 tunnel, which prevented it from ever operating. However, the elliptic cone was also designed to operate in the Mach 3.5 tunnel used for the circular cone experiments. A pending AFOSR proposal describes an experimental program for its use at the lower Mach number.			
14. SUBJECT TERMS		15. NUMBER OF PAGES	
		16. PRICE CODE	
17. SECURITY CLASSIFICATION OF REPORT UNCLASSIFIED		18. SECURITY CLASSIFICATION OF THIS PAGE UNCLASSIFIED	19. SECURITY CLASSIFICATION OF ABSTRACT UNCLASSIFIED
20. LIMITATION OF ABSTRACT			

JUN 21 2002

Final Report

AFOSR Grant F49620-98-1-0281  
05-1-0574

**CONTROLLED EXPERIMENTS ON  
INSTABILITIES AND TRANSITION TO TURBULENCE  
ON ELLIPTIC CONES AT HYPERSONIC MACH NUMBERS**

Thomas C. Corke

Clark Chair Professor  
University of Notre Dame  
Aerospace and Mechanical Engineering Department  
Center for Flow Physics and Control  
Hessert Center for Aerospace Research  
Notre Dame, IN 46556

**Executive Summary**

This work involved the study of instabilities and transition to turbulence in boundary layers on cones at different angles of attacks at high supersonic and hypersonic Mach numbers. It utilized facilities at NASA Langley Research Center which make use of "quiet" design nozzles to minimize the level of acoustic disturbances. The experiments involved two models. The first was a  $7^\circ$  half-angle circular cross-section cone designed by Cavalieri[1]. It was used in experiments at zero angle of attack[2, 3], where the principle instability is pairs of traveling oblique wave pairs; and at angles of attack where the principle instability is cross-flow modes. The circular cone at an angle of attack has a 3-D boundary layer which is similar to that on elliptic cone, which was the second model built. This consisted of a  $10^\circ$  half-angle cone with a 4:1 elliptic cross-section. The elliptic cone was designed to operate in a new Mach 8 tunnel at NASA Langley. It mounts on a sting which placed it inside the worst-case estimate of the location of the nozzle quiet zone. The model is annealed and hardened to withstand the  $900^\circ\text{F}$  free-stream temperature, and maintain a polished finish. A 3-D traversing mechanism capable of following the tapered elliptic surface, and operating at high temperatures in the hypersonic flow was also designed [4]. Unfortunately, the elliptic cone was never used because of technical problems with the Mach 8 tunnel which prevented it from ever operating. However, the elliptic cone was also designed to operate in the Mach 3.5 tunnel used for the circular cone experiments. A pending AFOSR proposal describes an experimental program for its use at the lower Mach number.

The research program focussed on the introduction of controlled disturbances to excite the most unstable linear instability modes, and on quantitative time-resolved measurements

of the instabilities for direct comparison to numerical simulations. Both of these were successfully completed. The controlled disturbances were based on phased plasma actuators. During the course of the research, these were perfected to operate for virtually infinite time without degradation. The time resolved measurements were made using hot-wires. For these we developed an in-situ calibration method to obtain the mean quantities,  $\overline{(\rho U)}$  and  $\overline{T_0}$ , and the fluctuating quantities  $\overline{(\rho U)'^2}$  and  $\overline{T_0'^2}$ . This was tested with the sharp-tipped circular cone at zero angle of attack in order to quantify the error in in-situ hot-wire calibration. These measurements also led to important parameters in the probe geometry that were needed to minimize its upstream influence in the subsonic portion of the boundary layer.

## Contents

1	Background	1
2	Experimental Approach	2
2.1	Cone Models	2
2.2	Plasma Actuator Array	3
2.3	Results: Circular Cone Actuation	6
2.4	In-situ Hot-Wire Calibration	8
3	Personnel and Technology Transfer	16
4	Summary	16

## 1 Background

In recent years there has been a renewed interest in clarifying the mechanisms of stability and transition to turbulence of high speed compressible boundary layers. Improved predictions of transition Reynolds numbers are needed in aeronautics applications such as high-speed vehicles or Earth re-entry systems. This motivation reflects the current evolution of the US Air Force from its static Cold War posture to one that is capable of projecting military power anywhere in the world at short notice, i.e. Global Reach, Global Power. The ability to formulate predictions of transition Reynolds numbers for high-speed flows on 3-D lifting bodies requires a fundamental understanding of the roles of instability mechanisms in transition behavior. In spite of its importance, there is very little accurate data with which to develop empirical criteria or to validate numerical simulations that might be used in design. To obtain this will require a concerted effort which involves a partnership between experimental and computational investigations. The challenge for experiments is to control unsteady initial conditions so that in direct comparisons to simulations, initial amplitudes and wave numbers can be specified. The outgrowth of such control is the potential to modify the transition front and therefore define initial conditions which can enhance performance by reducing drag and heat loading.

In all the past experiments, except those of Kosinov et al.[5] transition to turbulence developed from background disturbances. The problem with that approach is that the character of the free-stream disturbances (both vortical and acoustic) are difficult to completely document, and are largely facility dependent. In supersonic tunnels with free-stream Mach

numbers greater than 2, disturbances originate from side-wall boundary layers which are unstable and become turbulent. These are felt in the center of the nozzle as acoustic (Mach) waves. The “quiet” design supersonic nozzles [7] overcome this through a combination of wall suction at the throat, and well designed nozzle expansion sections which have curvature which maximizes the transition Reynolds number for a Goertler instability.

Even if the background disturbances are well documented, a second problem is that the manner by which free-stream disturbances enter and excite boundary layer modes (receptivity) is dependent on the model geometry such as local curvature, surface junctions, or imperfections (micro roughness).

Kosinov et al.[5] aimed at overcoming these problems by introducing periodic disturbances at a point on the surface of a flat plate at  $M = 2.0$ . The disturbances were produced by a glow-discharge between two electrodes in a small cavity below the plate surface. The forcing at a point produced a full spectrum of modes with different wave angles. Ultimately the most amplified mode was determined by the flow condition, and was in this regard, uncontrolled.

## 2 Experimental Approach

In this work, we have tried to develop an experimental analog to DNS calculations whereby we could specify the amplitudes, frequency, and wave angles of disturbances. The approach follows that used in numerous incompressible flows [6, 8] with the exception of the actuator. In order to minimize the required levels of controlled disturbances, the experiment was performed in the 0.5 m. Mach 3.5 “quiet” tunnel at NASA Langley Research Center.

### 2.1 Cone Models

The first model was a  $\phi_c = 7^\circ$  circular cone that is shown in Figure 1. The cone is 35.56 cm. in length. Its length was chosen to be compatible with the Mach 3.5 and 6<sup>1</sup> “quiet” tunnels at NASA Langley. At the typical stagnation pressures used in the past[3], the first 30.48 cm (86%) of the model is inside the “quiet zone.”

The circular cone is hollow with thin walls. It is instrumented with streamwise arrays of thermocouples and pressure ports. Wiring for the actuator array also run through the cone to an actuator hub which is 14.3 cm. from the cone tip. The cone tip is removable to allow different tip bluntness. The “sharp” tip has a nose radius of 0.038 mm.

The circular cone is supported by a sting which also holds a motorized 3-D traversing mechanism. The traversing mechanism holds removable wedges in which miniature pitot or hot-wire probes are held. Further details of the circular cone and traversing mechanism are given by Cavalieri[1].

The other model is a 4:1 elliptic cross-section cone. A photograph is shown in Figure 2. The angles of the major and minor axes are  $\phi_c = 10^\circ$  and  $2.65^\circ$ , respectively. This cone was originally designed for a Langley Mach 8 “quiet” tunnel which was never completed. It however is the same length (35.56 cm) as the circular cone, and will fit within the quiet zone in the Langley Mach 3.5 tunnel.

---

<sup>1</sup>This model was used once in this tunnel before it was dismantled at Langley. Efforts are being made to reopen this tunnel.

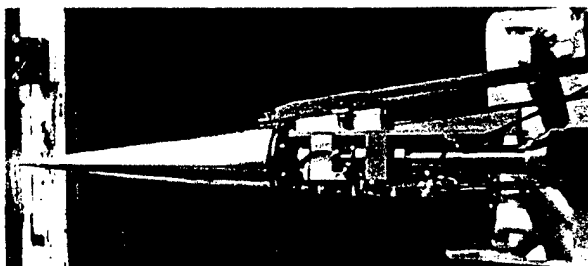


Figure 1: Photograph of circular cone and traversing mechanism shown outside of the 0.5 meter Mach 3.5 "quiet" tunnel at NASA Langley.



Figure 2: Photograph of the 4:1 elliptic cone and support sting.

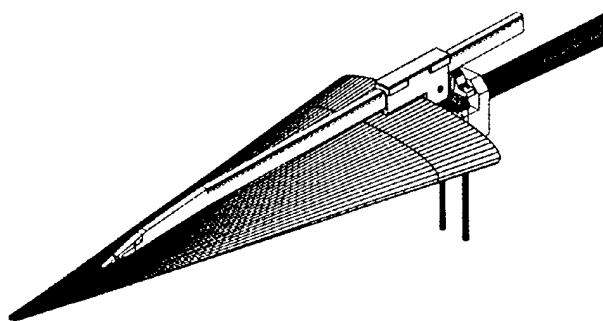


Figure 3: Illustration of traversing mechanism design for the elliptic cone.

The elliptic cone and sting are fabricated from 416 stainless steel and annealed and hardened to withstand up to 1360°R (the design stagnation temperature of the previously proposed Mach 8 tunnel). A design for a traversing mechanism has been developed by Siddiqi[4]. It is shown in the illustration in Figure 3.

## 2.2 Plasma Actuator Array

Our objective was to have actuators that could introduce periodic disturbances that would excite instability modes consisting of pairs of helical waves at the same frequency and equal-opposite wave angles.

Our approach was based on using an azimuthal array of disturbance actuators at one streamwise location [8]. Critical aspects of the design were the azimuthal spacing,  $s$ , of the array elements, and the streamwise location of the actuator on the cone. The ideal streamwise position of the actuator is near the location of the lower neutral branch of the linear stability growth curve. The choice of  $s$  is based on the range of frequencies and wave angles of the most amplified modes.

Linear stability calculations indicated that the most amplified dimensionless frequencies were in the range from  $10 \leq F \times 10^6 \leq 30$ , and had wave angles,  $\psi$ , of approximately 60°. In order to maximize the extent of the quiet zone, the experiment was designed to operate

Table 1: Excitation Conditions based on an azimuthal spacing of  $15^\circ$ 

$f$ (kHz)	$F \times 10^6$	$\psi$ ( $^\circ$ )	$n = 2\pi r_{actuator}/\lambda_\theta$
50	11.9	66	12
60	14.2	62	12
70	16.7	58	12

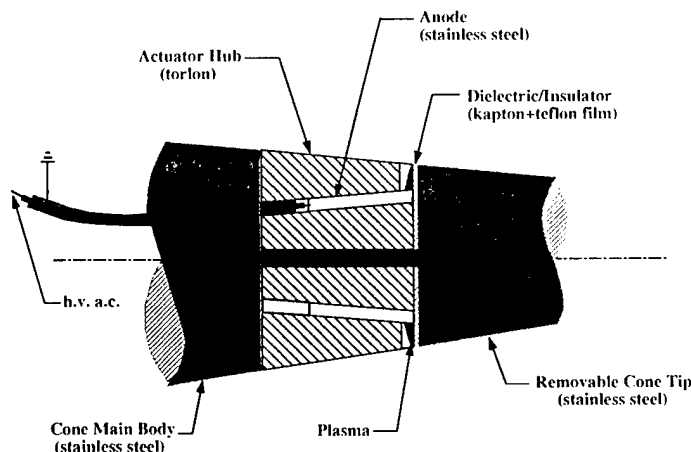
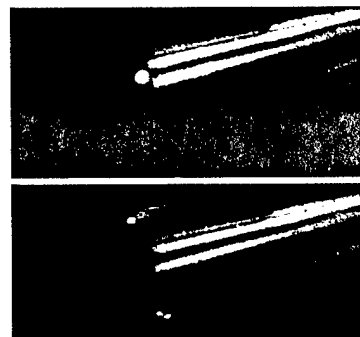


Figure 4: Cut-away illustration of plasma actuator hub used to excite T-S modes on circular cylinder.

Figure 5: Film clip of new actuator operating in a low pressure chamber with  $180^\circ$  phase shift between anodes.

at the lowest possible stagnation pressures. We chose  $P_0$  to be 172.35 kPa (25 psi.) At this value, and with  $T_0 = 311\text{K}$ , the actuator location of  $x = 14.303\text{ cm}$ . placed it just upstream of the lower neutral branch for the band of most amplified frequencies.

We chose an azimuthal spacing of  $15^\circ$  for the individual array elements. Based on this, Table 1 gives the largest wave angles that were possible for the range of frequencies used in the experiment.

The actuator is based on an a.c. glow discharge. A schematic cut-away drawing of the actuator hub is shown in Figure 4. The actuator is made up of azimuthally spaced anodes that are supplied with a high-voltage a.c. signal. The frequency of the a.c. matches the instability excitation frequency. The relative phase of the a.c. between adjacent anodes controls the instability wave angle. The metal tip of the cone is grounded and therefore forms a common cathode. When the voltage is high enough, ionized air (plasma) forms in the cavity. This results in a body force on the non-ionized air, which induces an unsteady jet of fluid that exits through the hole in the cone surface.

Figure 5 shows two frames of a film clip of the actuator operating in a low pressure chamber, which simulates the static pressure in the Mach 3.5 flow over the cone. In this case, the individual anodes were operated with a  $180^\circ$  phase shift. The plasma in the photographs appears blue.

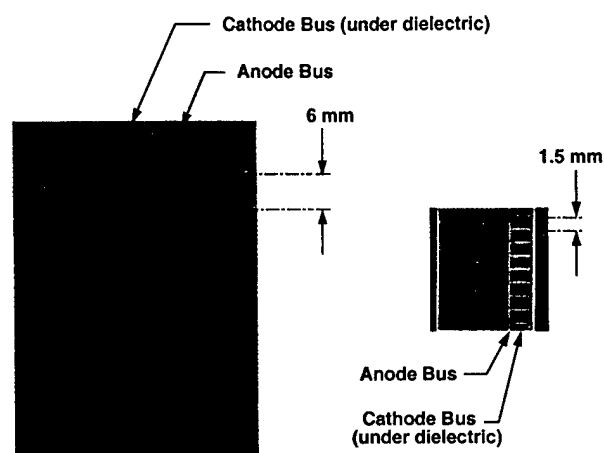


Figure 6: Photographs of two plasma actuators which were designed to excite different wavelengths of cross-flow modes on subsonic (left) and supersonic (right) swept wings.

A different plasma actuator has been designed for principally exciting stationary cross-flow modes. This would be used with the cylinder at an angle of attack, or with the elliptic cone.

The concept is based on the work of Saric *et al.*[9], in which the transition Reynolds number of 3-D boundary layers subject to a cross-flow instability, could be substantially increased by surface bumps which excite less amplified spanwise wave lengths. In association with Saric in joint DARPA funded research, we developed plasma actuators which could produce an effect equivalent to the surface bumps.

The actuators are fabricated on 0.1 mm thick F-4 grade fiberglass re-enforced epoxy strips which are copper clad on both sides (0.025 mm thick copper clad Kapton is also available). The copper is photo-etched to leave a pattern of conducting lines that serve as the anodes and cathodes. The surfaces are subsequently doped to leave a smooth uniform surface that is sanded smooth, with the electrodes flush to the surface.

The plasma forms at the edges of the anodes where they overlap the cathode. The body force is such that it induces a flow away from these edges. This results in a thinning of the boundary layer over the anodes, and a thickening of the boundary layer between the anodes. The wavelength of the alternate thickening and thinning is specified by the distance between anodes. The two actuators were designed for two swept wing experiments at ASU; for subsonic (left) and supersonic (right) wings. The advantage of the "plasma bumps" over fixed surface bumps is that the spacing can be modified to suit changes in the flight conditions. In addition, the plasma actuator can be operated to produce traveling disturbances which in the 3-D boundary layer, would excite traveling cross-flow modes. These are more amplified than the stationary modes, and would be preferred if a more rapid transition is needed. Finally, if conditions warrant, the actuator can be turned off, which is not possible with fixed surface bumps.

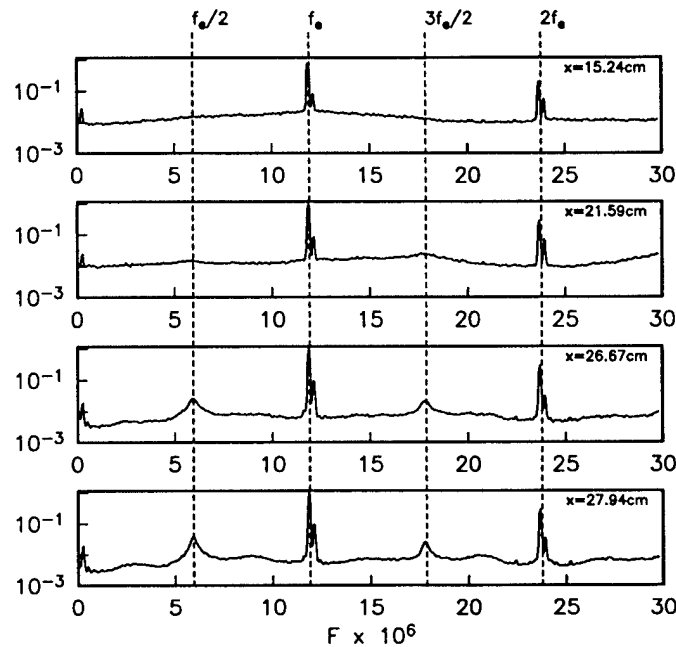


Figure 7: Spectra at different streamwise locations in the boundary layer, at a fixed height of  $y = 0.356$  mm., with excitation at 50kHz ( $F = 11.9$ ,  $\psi = \pm 66^\circ$ ).

## 2.3 Results: Circular Cone Actuation

All of the controlled instability results were for the circular cone at zero angle of attack. These used the actuator design which was illustrated in Figure 4. The excitation was designed to excite pairs of helical modes with azimuthal wave angles of  $\pm 66^\circ$ . The excitation frequency was 50kHz, which corresponds to the conditions in the top row of Table 1.

An example of the results with excitation are shown in Figure 7. The figure shows spectra at a fixed height in the boundary layer, and different downstream distances ( $15.24 \leq x \leq 27.94$  cm). The physical frequency is nondimensionalized as  $F = 2\pi f\nu/U^2$ .

The peaks at  $F = 11.9$  and  $23.8$  correspond to the excitation frequency ( $f_e$ ) and its harmonic ( $2f_e$ ), respectively. The most interesting feature of these spectra is the growth of a subharmonic of the excitation frequency ( $f_e/2$ ) at the further downstream positions. Along with the subharmonic peak, a peak at  $3f_e/2$  is also observed. This likely evolves from a summing interaction between the fundamental and subharmonic modes.

In order to better understand the origin of the subharmonic, the effect of changing the initial 50kHz amplitude was investigated. This is shown in the top part of Figure 8. This was documented at  $x = 23.5$  cm.,  $y = 0.356$  mm. and  $\theta = 0^\circ$ . Here the initial amplitude above a minimum to produce a plasma, was varied by a factor of approximately two. The abscissa corresponds to the measured amplitude at the fundamental frequency normalized by its minimum value. The accuracy of the amplitude is 0.05 percent of the maximum value.

The ordinate in the plot is the normalized amplitude at the subharmonic frequency on a log axis. If the subharmonic mode results from a secondary interaction with the fundamental, we expect it to have an exponential response to the fundamental mode amplitude. The results seem to support this, since the points fall on a straight line on a log axis.

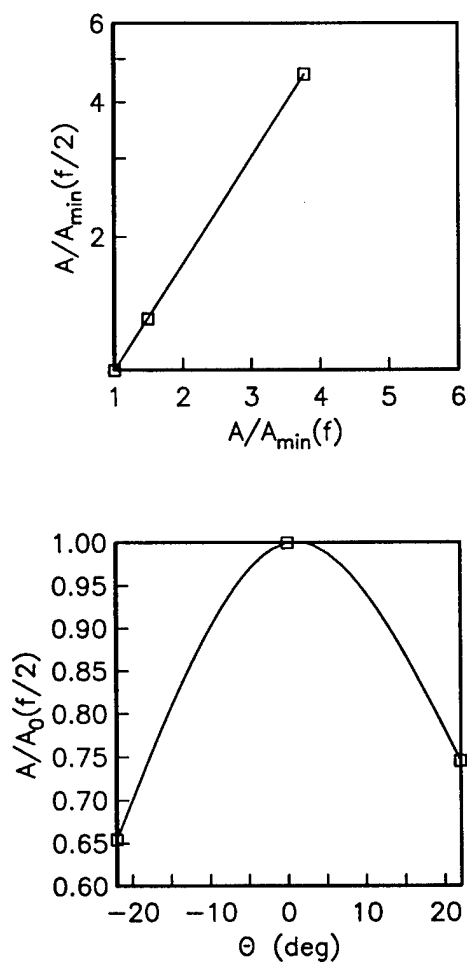


Figure 8: Response of the subharmonic mode to different fundamental mode amplitudes (top), and subharmonic amplitude azimuthal variation (50kHz excitation measured at  $x = 23.5$  cm.,  $y = 0.356$  mm.).

Measurements were taken at different azimuthal positions to determine the azimuthal wave length of the subharmonic mode. The result is shown in the lower plot in Figure 8. This corresponds to the same spatial position as before. The azimuthal angle ranges from  $\pm 25^\circ$  with respect to the  $0^\circ$  reference position used in the previous figures. The accuracy in the azimuthal position is  $0.56^\circ$ . The subharmonic amplitude has been normalized by the value at  $\theta = 0^\circ$ .

The azimuthal amplitude variation for helical mode pairs should consist of periodic maxima and minima. For the  $n = 12$  fundamental mode that was excited, amplitude minima should occur approximately  $30^\circ$  apart. A secondary instability analysis in the boundary layer on a flat plate at Mach 1.6 by Ng and Zang<sup>7</sup> which specified a primary instability of pairs of oblique waves at a fundamental frequency, found the most amplified subharmonic consisted of pairs of oblique waves of comparable wave angles. This appears to be consistent with the spacing of the minima for the subharmonic mode in our experiment.

The results in the previous two figures were all based on time series obtained from a hot-wire which was uncalibrated, but operated at a fixed high overheat so that it should be primarily sensitive to mass-flux fluctuations. This is a limitation of these measurements which we address with a new in-situ calibration approach that was developed as part of this grant.

## 2.4 In-situ Hot-Wire Calibration

To our knowledge, there has never been a successful attempt to measure amplification rates with calibrated hot-wires in supersonic boundary layers. Typically, un-calibrated wires are used, with the assumption that when maintained at a high enough overheat, the wire becomes mostly sensitive to mass-flux fluctuations and the amplification rate of linear modes can be deduced by comparing voltage fluctuation magnitudes at different spatial locations. With un-calibrated sensors, this requires that at every measurement station, the wire is placed at a point within the boundary layer where the mean mass-flux is constant to ensure that the dynamic sensitivity remains fixed. The difficulties associated from trying to infer amplification rates with un-calibrated sensors becomes more severe when trying to measure nonlinear disturbances, such as the development of sub-harmonic resonance that we observed [3] in Figure 7.

The appearance of these resonant modes, resulting from non-linear interactions with the linear modes, stresses the need for calibrated time-resolved measurements. Our efforts in the last year of the grant had therefore been directed towards developing an “in-situ” approach to hot-wire calibration, which is described in the following.

The standard approach to calibration involves placing the hot-wire in the free-stream at a fixed Mach number while changing stagnation pressure ( $P_o$ ) and temperature ( $T_o$ ) (hence mass flux) at multiple overheats. However, this may not be feasible in all facilities with limited control over  $P_o$  and  $T_o$ . We should also stress that many calibration data pairs are needed to achieve an accurate calibration which is suitable for measurement of fluctuation amplitudes.

Consequently, an approach has been developed that simultaneously calibrates a hot-wire while performing wall-normal surveys of the fluctuating flow-field. This approach is termed “in-situ” calibration, and makes use of the variation of  $P_o$  and  $T_o$  within the boundary layer. This is done by performing total-pressure surveys with a miniature probe to obtain Mach number profiles. Subsequently, a hot-wire is traversed through the layer at multiple

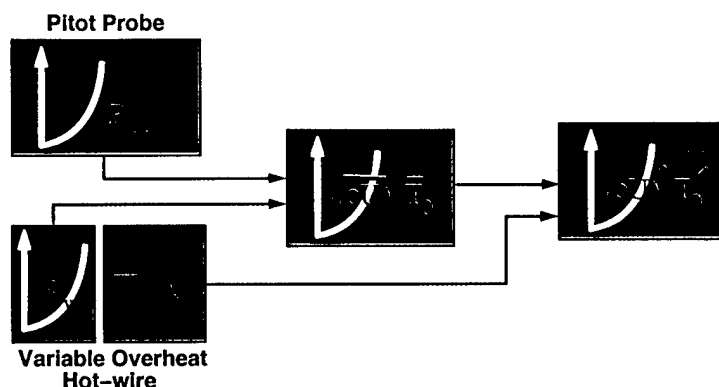


Figure 9: Schematic of process for in-situ hot-wire calibration.

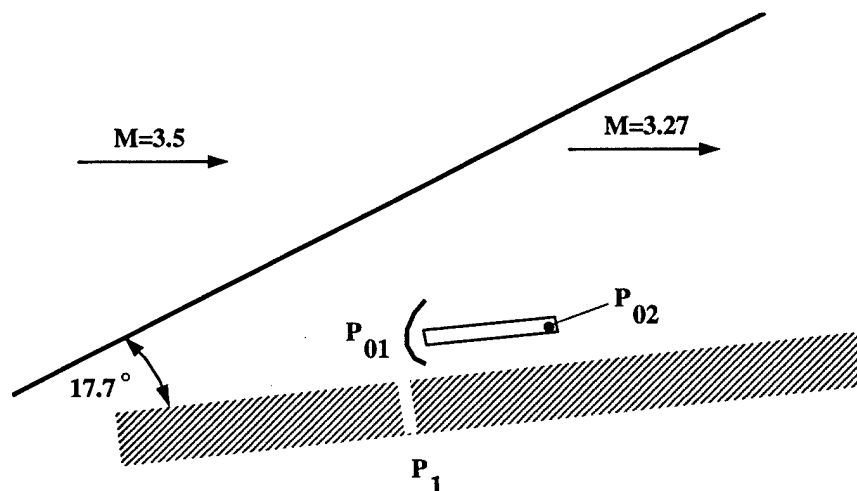


Figure 10: Schematic for determining local Mach number profile in the boundary layer.

overheats. At the lowest overheat, the wire measures the stagnation temperature, which together with the previously established Mach profile provides the mean mass-flux and  $T_o$  required for the calibration. This is illustrated in the schematic in Figure 9.

This calibration technique was carried out in the boundary layer over the circular cone at zero angle of attack at Mach 3.5. This case was selected because we could easily solve the mean flow similarity solution for this conic flow and determine the error in our measurements. It begins with the measurement of the Mach number profile at an  $x$ -station in the boundary layer. For this, the static pressure is measured using a wall pressure port in the model, and the total pressure is measured with a miniature pitot probe that is traversed through the layer. This is illustrated in Figure 10.

The Mach number profile is found from a recursive solution to the identity

$$P_{02} = \underbrace{\frac{P_{02}}{P_{01}}}_{\mathcal{F}(M)} \underbrace{\frac{P_{01}}{P_1}}_{\mathcal{F}(M)} P_1.$$

This step represents the upper-left box in Figure 9.

This profile is repeated at the same heights above the wall with a hot-wire which is operated at different (10 or more) over-heat values. The stagnation temperature,  $T_0$ , is found from the hot-wire at zero overheat (cold-wire). Based on the resistive-temperature properties of the wire material, the wire temperature is

$$T_w = T_{ref} + \left(1 + \alpha \frac{R}{R_{ref}}\right). \quad (1)$$

Then the stagnation temperature is

$$T_0 = T_w / \eta \quad (2)$$

where  $\eta$  is the recovery factor.

Knowing  $T_0$ , the static temperature is found from

$$T = \frac{T_0}{1 + \frac{\gamma-1}{\gamma} M^2}. \quad (3)$$

Finally, the mass flux profile is found from

$$\overline{(\rho U)} = \frac{P_0 M}{\sqrt{T}} \sqrt{\frac{\gamma}{R}}. \quad (4)$$

Implicit in the in-situ calibration approach is the need to accurately measure the mean quantities through the boundary layer. A somewhat unexpected issue that emerged in this was the effect of probe interference. An example is shown in Figure 11. Here we observed two deviations in the measured values from the theoretical distribution: an over-shoot at the edge of the boundary layer, and an under-shoot in the lower part of the layer.

These two types of experimental deviations had previously been observed by Kendall[10] and Morkovin and Bradfield[11]. In both cases it was associated with probe interference. At the outer edge of the boundary layer, Kendall could eliminate the overshoot when the pitot probe diameter was no larger than 12 percent of the boundary layer thickness. Morkovin and Bradfield associated the deviation in the lower part of the boundary layer with an upstream rise in the static pressure produced by the sensor and communicated upstream in the subsonic portion of the boundary layer. They recommended an upstream influence distance,  $s$ , where the pressure disturbance diminishes by  $e^{-1}$  given as

$$s = \frac{1.3}{\sqrt{M^2 - 1}} \frac{T_w}{T_e} R_x^{1/6} s^{-1/3} - \frac{M^2 + 2}{2\sqrt{M^2 - 1}} \left(\frac{T_w}{T_e}\right)^{0.7}. \quad (5)$$

For our experimental conditions,  $s \simeq 10\delta$ .

The recommendations from these early investigations was used to obtain the results shown in Figure 12. In this case, the pitot tube exterior dimensions were 0.203 mm. wide by 0.102 mm. high (0.008 in. wide by 0.004 in. high). For a nominal boundary layer thickness, the probe height was approximately  $0.08\delta$ , which satisfied Kendall's[10] guideline. The probe extended 1.27 cm. (0.5 in.) upstream of the probe support wedge. This corresponds to approximately  $10\delta$  in accordance with the Morkovin and Bradfield[11] guidelines. A photograph of the final arrangement is shown in Figure 13. The tubulation used is designated as "e".

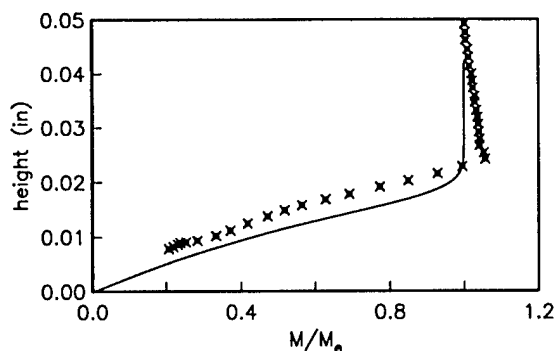


Figure 11: Mach number profile at one  $x$ -location in the boundary layer over the circular cone.  $M = 3.5$ ,  $\alpha = 0$ . Solid curve is theoretical profile.

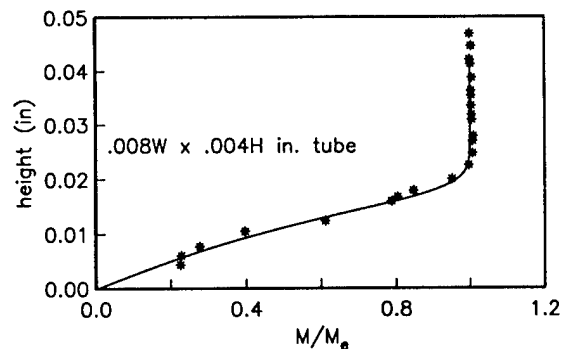


Figure 12: Mach number profile at one  $x$ -location in the boundary layer over the circular cone measured with minimum probe interference.  $M = 3.5$ ,  $\alpha = 0$ . Solid curve is theoretical profile.

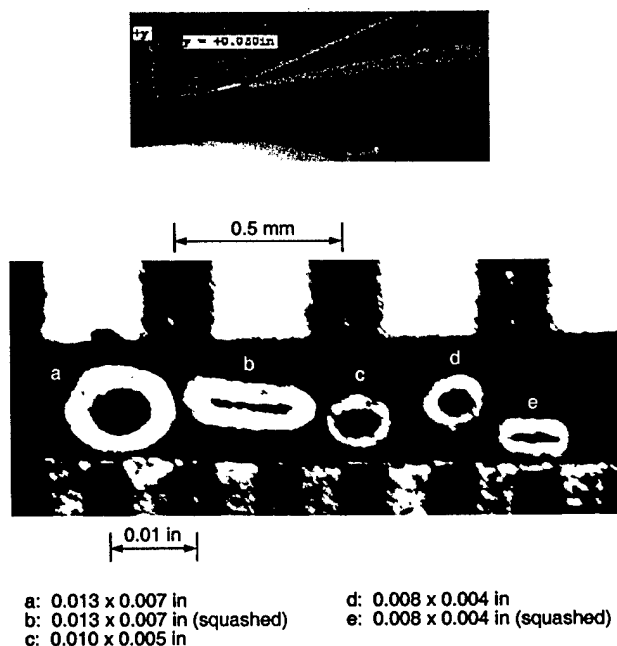


Figure 13: Photographs of probe support wedge with pitot probe at tip, and cross-sections of tubulations used to measure Mach number profiles. Results in Figure 12 used tubing "e".

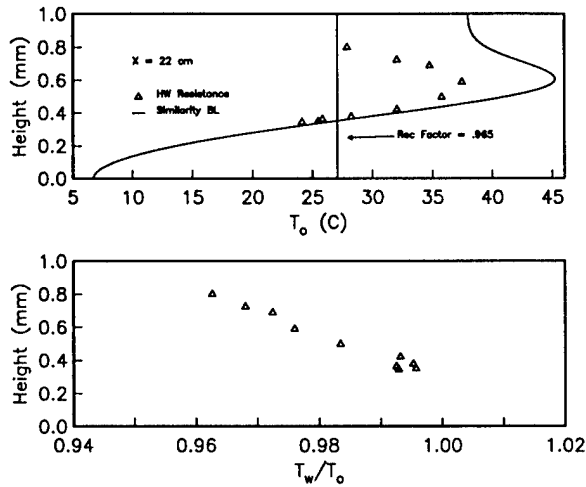


Figure 14: Comparison of the cold-wire temperature through the boundary layer against theoretical  $T_0$  profile (top). Variation in recovery factor through the boundary layer (bottom).

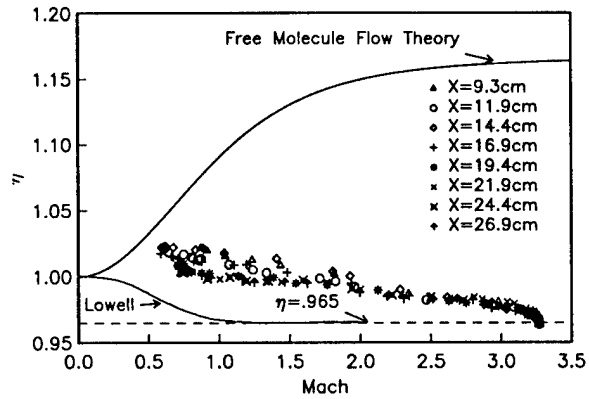


Figure 15: Recovery factor based on all measured profiles over the circular cone. Curves represent free molecular limit and Lowell continuum model.

Figure 12 demonstrates that when following the guidelines, it was possible to accurately measure the mean Mach number profiles. Of the two criteria, the Morkovin and Bradfield[11] is the most difficult to satisfy since it is a function of local flow properties ( $R_x, M, T_w/T_e$ ). Therefore information about the mean flow needs to be known to some extent in order to properly design probes. This also applies to the hot-wire probes. We have experimentally determined that when our hot-wire probes are designed by the same criteria as the pitot probe, the upstream effect, measured as a local change in the wall static pressure, is comparable to the pitot probe. Therefore we expect similar accuracy with the properly designed hot-wire probes.

The hot-wire, operating at zero overheat (cold wire) was used to measure the  $T_0$ . A question that arises at this point is the value of the recovery factor,  $\eta$ . This was investigated by comparing the wall-normal profile of  $T_w$  in the boundary layer against the theoretical distribution of  $T_0$ . This is shown in Figure 14. The value of  $\eta$  which most often appears in the literature is 0.965. As these results indicate, the recovery factor is not constant, but varies through the layer. This was compiled for all of the  $x$  locations in Figure 15. This indicates that  $\eta$  varies from approximately 1.02 to 0.965. We have shown that assuming a constant value for  $\eta$  in this range accounts for at most a 3% error in the mass flux.

Knowing  $T_0$  and  $M$ , Eqs[3 and 4] are used to determine  $(\rho\bar{U})$ . A sample of the measurements obtained from the pitot probe is shown as the square symbols in Figure 16. The solid curve is the theoretical profile.

The approach to calibrate the hot-wire is to decompose the anemometer mean voltages,  $\bar{V}_o$ , into  $(\rho\bar{U})$  and  $\bar{T}_0$  through calibration for many (typically 10) over-heats. The hot-wire is operated in a constant current mode and frequency compensated.

Analysis of the steady heat transfer balance for the hot-wire operating in a constant

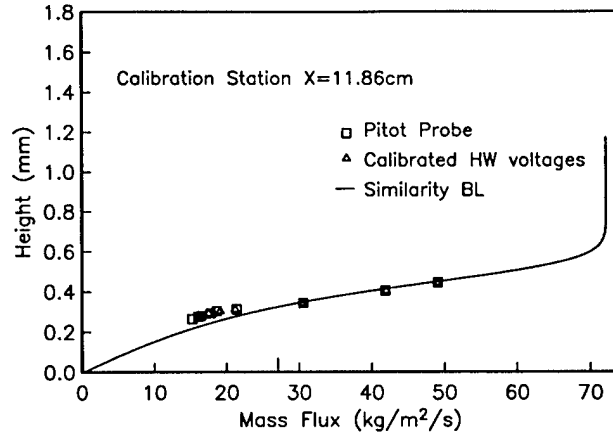


Figure 16: Profile of  $(\rho U)$  through the boundary layer for the circular cone measured using the pitot probe and cold-wire (square symbols), and measured using the calibrated hot-wire (triangle symbols) Solid curve is the theoretical profile.

current mode leads to the following equation

$$C_1 \bar{T}_0^a \bar{V}_o + C_2 \bar{T}_0^a - C_3 \bar{T}_0^{1+a} + C_4 \bar{V}_o (\rho U)^n \bar{T}_0^{a-an} + C_5 (\rho U)^n \bar{T}_0^{a-an} - C_6 (\rho U)^n \bar{T}_0^{1+a-an} - C_7 \bar{V}_o = 0 \quad (6)$$

where  $n$  and  $a$  are known constants, and  $C_1 \dots C_7$  are coefficients to be determined from calibration at different over-heats.

The problem is formulated to minimize the least-squared error. This leads to the following general matrix, where  $a_{1i}^j \dots a_{7i}^j$  represent the terms multiplied by the respective coefficients for the  $i$ th  $[(\rho U), \bar{T}_0]$  data pair, and the  $j$ th overheat.

$$\begin{bmatrix} \sum_i (a_{1i}^2)^j & \sum_i (a_{1i} a_{2i})^j & \sum_i (a_{1i} a_{3i})^j & \dots & \sum_i (a_{1i} a_{7i})^j \\ \sum_i (a_{1i} a_{2i})^j & \sum_i (a_{2i}^2)^j & \sum_i (a_{2i} a_{3i})^j & \dots & \sum_i (a_{2i} a_{7i})^j \\ \sum_i (a_{1i} a_{3i})^j & \sum_i (a_{2i} a_{3i})^j & \sum_i (a_{3i}^2)^j & \dots & \sum_i (a_{3i} a_{7i})^j \\ \vdots & \vdots & \vdots & \ddots & \vdots \\ \sum_i (a_{1i} a_{7i})^j & \sum_i (a_{2i} a_{7i})^j & \sum_i (a_{3i} a_{7i})^j & \dots & \sum_i (a_{7i}^2)^j \end{bmatrix} \begin{bmatrix} (C_1)^j \\ (C_2)^j \\ (C_3)^j \\ \vdots \\ (C_7)^j \end{bmatrix} = \begin{bmatrix} 0 \\ 0 \\ 0 \\ \vdots \\ 0 \end{bmatrix} \quad (7)$$

With the coefficients determined from the calibration, the time averaged voltages at each spatial point from the hot-wire can be decomposed into  $(\rho U)$  and  $\bar{T}_0$  by solving the following matrix.

$$\begin{bmatrix} \sum_j m_{1j}^2 & \sum_j m_{1j} m_{2j} & \dots & \sum_j m_{1j} m_{4j} \\ \sum_j m_{2j} m_{1j} & \sum_j m_{2j}^2 & \dots & \sum_j m_{2j} m_{4j} \\ \vdots & \vdots & \ddots & \vdots \\ \sum_j m_{4j} m_{1j} & \sum_j m_{4j} m_{2j} & \dots & \sum_j m_{4j}^2 \end{bmatrix} \begin{bmatrix} \bar{T}_0^a \\ \bar{T}_0^{1+an} \\ (\rho U)^n \bar{T}_0^{a-an} \\ (\rho U)^n \bar{T}_0^{1+a-an} \end{bmatrix} = \begin{bmatrix} -\sum_j m_{1j} m_{5j} \\ -\sum_j m_{2j} m_{5j} \\ \vdots \\ -\sum_j m_{4j} m_{5j} \end{bmatrix} \quad (8)$$

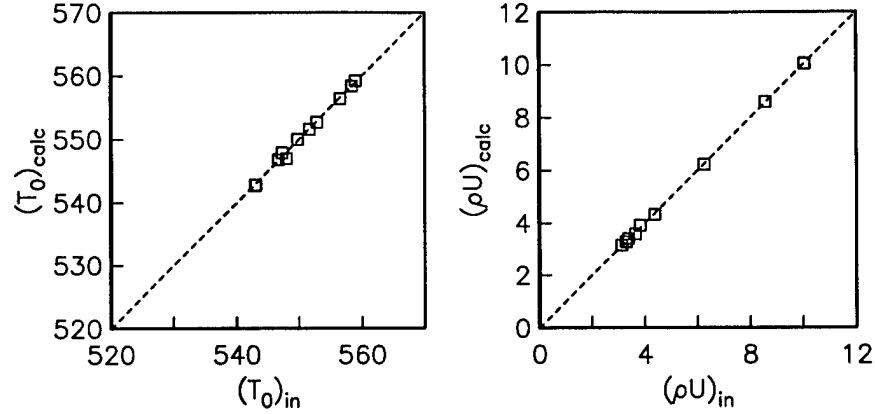


Figure 17: Calibration quantities output using Eq[6] versus input for the hot-wire.

where  $m_{1j} = C_{1j}\bar{V}_o^j + C_{2j}$ ,  $m_{2j} = C_{3j}$ ,  $m_{3j} = C_{4j}\bar{V}_o^j + C_{5j}$ ,  $m_{4j} = C_{6j}$  and  $m_{5j} = C_{7j}\bar{V}_o^j$ . Again,  $j$  represents the over-heat values used in calibration.

An example of the calibration is shown in Figure 17. This shows the calibration data versus the values obtained from the calibration relation (Eq[6]). The input-output relation falls on a straight line indicating perfect agreement.

A further indication of the calibration comes from comparing the  $(\bar{\rho U})$  variation across the boundary layer with the theoretical profile. This is shown as the triangle symbols in Figure 16. The error in the hot-wire distribution is identical with that of the pitot probe. Since one was used to calibrate the other, this indicates a perfect calibration result. If the theoretical distribution had been used to supply the calibration data pairs, the comparison to theory could have been perfect. However, since the theoretical distribution may not always be known, we chose to use calibration data from the pitot probe as a complete test of the in-situ calibration approach.

Ultimately, as illustrated in Figure 9, the calibrated hot-wire is intended for time-resolved measurements such as the variance of the fluctuating flow quantities,  $(\bar{\rho U})'^2$  and  $\bar{T}_0'^2$  in terms of the variance of the anemometer voltage,  $\bar{V}_o'^2$ .

In order to relate these statistics to the anemometer voltage fluctuations, Eq[6] is rewritten in a more general form as

$$C_1 T_0^a V_o + C_2 T_0^a - C_3 T_0^{1+a} + C_4 V_o (\rho U)^n T_0^{a-an} + C_5 (\rho U)^n T_0^{a-an} - C_6 (\rho U)^n T_0^{1+a-an} - C_7 V_o = 0 \quad (9)$$

For this, we substitute for  $T_0$ ,  $(\rho U)$  and  $V_o$  in terms of the following decompositions

$$T_0 = \bar{T}_0 + T_0' \quad (10)$$

$$(\rho U) = (\bar{\rho U}) + (\rho U)' \quad (11)$$

$$V_o = \bar{V}_o + V_o' \quad (12)$$

where the primed terms represent the mean-removed fluctuations of each of the quantities.

After substitution, the equation is expanded and linearized. Within this equation, the mean equation (Eq[6]) is identically zero. This leaves the following

$$q_1 V_o' + q_2 (\rho U)' + q_3 T_0' \quad (13)$$

where

$$q_1 = C_1 \bar{T}_0^a + C_4 (\bar{\rho U})^n \bar{T}_0^{a-an} - 1 \quad (14)$$

$$q_2 = C_4 n \bar{V}_o (\bar{\rho U})^{n-1} \bar{T}_0^{a-an} + C_5 n (\bar{\rho U})^{n-1} \bar{T}_0^{a-an} - C_6 n (\bar{\rho U})^{n-1} \bar{T}_0^{1+a-an} \quad (15)$$

$$q_3 = C_1 a \bar{T}_0^{a-1} \bar{V}_o + C_2 a \bar{T}_0^{a-1} - C_3 (1+a) \bar{T}_0^a + C_4 (a-an) \bar{V}_o (\bar{\rho U})^n \bar{T}_0^{a-an-1} + \\ C_5 (a-an) (\bar{\rho U})^n \bar{T}_0^{a-an-1} - C_6 (1+a-an) (\bar{\rho U})^n \bar{T}_0^{a-an}. \quad (16)$$

Taking the variance of the terms in Eq[13] and rearranging gives the following

$$\overline{V_o'^2} = \left( \frac{q_2}{q_1} \right)^2 \overline{(\rho U)'^2} + \left( \frac{q_3}{q_1} \right)^2 \overline{T_0'^2} + 2 \frac{q_2}{q_1} \frac{q_3}{q_1} \overline{(\rho U)' T_0'}. \quad (17)$$

As a general form, Eq[17] can be written as

$$k_1 D_1 + k_2 D_2 + k_3 D_3 - k_0 = 0 \quad (18)$$

where

$$k_1 = \left( \frac{q_2}{q_1} \right)^2 \quad k_2 = \left( \frac{q_3}{q_1} \right)^2 \quad k_3 = 2 \frac{q_2}{q_1} \frac{q_3}{q_1}$$

which are functions of the sensor overheat, and

$$D_1 = \overline{(\rho U)'^2} \quad D_2 = \overline{(\rho U)' T_0'} \quad D_3 = \left( \frac{q_3}{q_1} \right)^2 \overline{T_0'^2}$$

which are the unknown variances of the flow quantity fluctuations.

The unknown quantities ( $D$ s) are found by minimizing the least-square-error defined as

$$\sigma^2 = \sum_{j=1}^N [k_{1j} D_1 + k_{2j} D_2 + k_{3j} D_3 - k_{0j}]^2 \quad (19)$$

where as before,  $j$  represents the sensor overheat values.

The unknowns are then found by solving the following matrix

$$\begin{bmatrix} \sum_j (k_{1j}^2) & \sum_j (k_{1j} k_{2j}) & \sum_j (k_{1j} k_{3j}) \\ \sum_j (k_{1j} k_{2j}) & \sum_j (k_{2j}^2) & \sum_j (k_{2j} k_{3j}) \\ \sum_j (k_{1j} k_{3j}) & \sum_j (k_{2j} k_{3j}) & \sum_j (k_{3j}^2) \end{bmatrix} \begin{bmatrix} \overline{(\rho U)'^2} \\ \overline{(\rho U)' T_0'} \\ \overline{T_0'^2} \end{bmatrix} = \begin{bmatrix} -\sum_j m_{0j} m_{1j} \\ -\sum_j m_{0j} m_{2j} \\ -\sum_j m_{0j} m_{3j} \end{bmatrix}$$

### 3 Personnel and Technology Transfer

This research was performed by Professor Thomas Corke along with two graduate assistants. It benefited from the interaction of Mr. Steve Wilkinson at NASA Langley Research Center who coordinated the Mach 3.5 tunnel experiments, as well as made a tireless effort to complete the Mach 8 tunnel.

This work will lead to a Ph.D. thesis by Mr. Eric Matlis. He is expected to defend his thesis in the December, 2002. The other graduate student working under this grant developed the final design of the actuator. She completed a M.S. thesis[12] in August, 2001, and is presently pursuing a Ph.D. at Notre Dame.

In addition to the theses, one paper has been published[3], and two are in progress related to the plasma actuator, and in-situ hot-wire calibration method.

There have been numerous spin-offs of the plasma actuator technology that was developed under this grant and a DARPA grant. This includes separation control on helicopter rotors (DARPA/AR0) and on LPT blades in turbo-jet engines (NASA Glenn), control of jet flows to reduce sound (NASA Langley), lift enhancement (AFIT)[13], control of cross-flow instabilities in high-speed flows (ASU/DARPA), and trajectory control of missiles (EglinAFB/AFRL).

As a result of this work, Eric Matlis was named a 2002 NASA Graduate Fellow. He will continue the work developed in this grant in further experiments with the two cone models in the Mach 3.5, and possibly a Mach 6, "quite" tunnel at NASA Langley. Dr. Meelan Choudhari, in the LaRC Computational Modeling and Simulation Branch, will coordinate a parallel numerical study which will be used for experimental design and provide a basis for experimental/computational validation.

### 4 Summary

The research program was designed to add to our understanding of transition to turbulence over 3-D supersonic/hypersonic lifting bodies. It brought together for the first time, two necessary capabilities:

1. the ability to control the steady and unsteady initial conditions of instabilities leading to transition to turbulence, and
2. accurate time-resolved measurements of flow quantities in compressible boundary layers using calibrated hot-wire sensors.

In addition, it teamed efforts in experiments and computations, with the computations first guiding the design and accuracy of measurements, and experiments ultimately providing validation of the numerical simulations.

Finally, the approaches that were developed for controlling initial conditions in our laboratory experiments have the potential to be used in real applications in transition control, as well as numerous other flow control applications.

## References

- [1] Cavalieri, D. A. 1995. On the Experimental Design for Instability Analysis on a Cone at Mach 3.5 and 6 Using a Corona Discharge Perturbation Method. M.S. Thesis, Illinois Institute of Technology.
- [2] Corke, T. C. & Cavalieri, D. A. 1997. Controlled Experiments on Instabilities and Transition to Turbulence in Supersonic Boundary Layers. *AIAA 97-1817*.
- [3] Corke, T.C., Cavalieri, D. A. and Matlis, E. 2002. Boundary layer instability on a sharp cone at Mach 3.5 with controlled input. *AIAA J.*, **40**, 5, p. 1018.
- [4] Siddiqi, M. A. H. 1996. Design of elliptic cone and traverse mechanism for transition studies in Mach 8 flow. M.S. Thesis, Ill. Inst. of Tech., Chicago, Illinois.
- [5] Kosinov, A., Maslov, A., and Shevelkov, S. 1990. Experiments on the Stability of Supersonic Laminar Boundary Layers. *J. Fluid Mech.*, **219**, p.621.
- [6] Corke, T. C. and Mangano, R. A., 1989. Resonant Growth of Three-dimensional Modes in Transitioning Blasius Boundary Layers. *J. Fluid Mech.*, **209**, p.93-150.
- [7] Wilkinson, S. P., Anders, S. G., Chen, F. J. and Beckwith, I. E. 1992. Supersonic and Hypersonic Quiet Tunnel Technology at NASA Langley. *AIAA Paper No. 92-3908*.
- [8] Corke, T. C. and Kusek, S. M. , 1993. Resonance in Axisymmetric Jets with Controlled Helical-mode Input. *J. Fluid Mech.*, **249**, p.307-336.
- [9] Saric, W., Carillo, R., & Reibert, M. 1998. Leading-edge roughness as a transition control mechanism. *AIAA 98-0781*.
- [10] Kendall, J. 1957. *J. Aero. Sci.*
- [11] Morkovin, M. & Bradfield, W. 1954. *J. Aero. Sci.*
- [12] Post, M. L. 2001. Phased plasma actuators for unsteady flow control. M.S. Thesis, University of Notre Dame.
- [13] Corke, T., Jumper, E., Post, M., Orlov, D. and McLaughlin, T. 2002. Application of weakly-ionized plasmas as wing flow-control devices. Aerospace Sciences Meeting Paper AIAA-2002-0350 (submitted to AIAA J.).